PAPER

A novel CoFe$_2$O$_4$@Cr-MIL-101/Y zeolite ternary nanocomposite as a magnetically separable sonocatalyst for efficient sonodegradation of organic dye contaminants from water†

Meysam Sadeghi, Saeed Farhadi [iD] * and Abedin Zabardasti [iD]

In this research, a novel magnetic sonocatalyst nanocomposite, CoFe$_2$O$_4$@Cr-MIL-101/Y zeolite, has been successfully fabricated employing a simple hydrothermal method. The as-prepared catalyst was thoroughly identified using Fourier transform infrared spectroscopy (FTIR), X-ray diffraction (XRD), field emission scanning electron microscopy (FESEM), energy dispersive X-ray spectroscopy (EDS), EDS elemental dot-mapping, transmission electron microscopy (TEM), atomic force microscopy (AFM), vibrating sample magnetometer (VSM), and nitrogen Brunauer–Emmett–Teller (N$_2$-BET) analyses. The procured CoFe$_2$O$_4$@Cr-MIL-101/Y nanocomposite was then assessed for the decomposition of three types of organic dyes namely methylene blue (MB), rhodamine B (RhB) and methyl orange (MO) from water solution using ultrasound irradiation and subsequently monitored *via* UV-Vis absorption technique. The sonodecomposition reactions of organic dyes were accomplished in the presence of the H$_2$O$_2$ solution as a green oxidizing agent. Furthermore, the influence of various experimental independent factors such as irradiation time, process type, initial dye concentration, catalyst dosage, H$_2$O$_2$ concentration, scavenger type, and catalyst regeneration on the decomposition of MB, RhB and MO were surveyed. Additionally, a first order kinetic model was applied to investigate the sonodecomposition reactions of dye contaminants. The rate constant (k) and half-life ($t_{1/2}$) data were gained as 0.0675 min^{-1} and 10.2666 min, respectively, for the decomposition of MB in the US/H$_2$O$_2$/CoFe$_2$O$_4$@Cr-MIL-101/Y system. Besides, evaluating the attained results, the distinctive performance of ˙OH as the radical scavenger originating from H$_2$O$_2$ throughout the sonodecomposition process is vividly approved.

1. Introduction

In recent years, the numbers of major health and environmental dilemmas have been growing from day to day due to the release of tremendous amounts of chemicals into the environmental zones like water, soil, air and so on.[1] As industrial activities are spreading all over the world, it will be much harder to protect natural and environmental sources against drastic quantities of chemicals which plummet from these units. Also, it has been revealed that there are more than 10 000 different kinds of dyes and pigments, approximately 700 000 tons of which are produced yearly.[2] On the other hand, more than 200 000 tons (about 10–15%) of residual synthetic dyes are discarded from the textile mills dyeing processes and between 2 to 10% of them are directly evacuated into the sewage systems.[3] The improper evacuation of organic dye sewages into water

supplies and the environment without any remediation can cause serious and irreparable consequences for the human body and environmental species. The permanent exposure to such organic dye contaminants even at low concentrations has proven to be harmful owing to their bioaccumulation in living tissues through skin, eyes, inhalation and unclean drinking water.[4] Therefore, these sorts of organic contaminants with carcinogenic and mutagenic effects referred to the existence of various aromatic compounds mostly naphthalene, benzidine within their structures, should be scrupulously disposed or removed from wastewater systems prior to their entrance into the environment.[5–7] From the other point of view, there are diverse methodologies to eradicate contaminant dye molecules from aqueous solutions such as ultrasonic degradation,[8] adsorption,[9,10] photocatalytic treatment,[11] biodegradation,[12] electrochemical oxidation,[13] *etc.* Among them, the sonodecomposition reaction has been exerted as a significant, effective and environmentally friendly process to eliminate dye contaminants through the formation of ˙OH (hydroxyl) and ˙H (proton) radicals and a series of other species like HOO˙ (perhydroxyl) radicals, O$_2$, *etc.*[14] Furthermore, the versatile sorts of

Department of Chemistry, Lorestan University, Khorramabad, 68151-44316, Iran. E-mail: farhadi.s@lu.ac.ir; sfarhadi1348@yahoo.com; Fax: +98 6633120618; Tel: +98 6633120611

† Electronic supplementary information (ESI) available. See DOI: 10.1039/d0ra00877j

catalysts, including $CuFe_2O_4/MIL-101/Graphene,$[15] $TiO_2/mont-morillonite,$[16] Yb, B and Ga dopted $Er^{3+}:Y_3Al_5O_{12}/TiO_2,$[17] $CoFe_2O_4@ZnS,$[18] $Au/NiGa_2O_4–Au–Bi_2O_3,$[19] $CoFe_2O_4/CdS,$[20] $InVO_4/TiO_2,$[21] $CeO_2/TiO_2,$[22] $MgO,$[23] $WO_3,$[24] $AgBr,$[25] and some others, have been applied to remove dye contaminants through the sonodecomposition activities. In addition to this, metal–organic frameworks (MOFs) are introduced as one of the new kind of organic–inorganic materials.[26] Among all types of MOFs, Cr-MIL-101 (with a band gap energy 2.06 eV)[27] has attracted special attention because of its prominent chemical and physical features.[28,29] Moreover, as it has been lucratively applied in different fields of research like gas sensing procedures, separation and catalysis,[30–32] it counts as a promising candidate for the removal of organic dyes. It is also noticeable that the zeolites are known as a subgroup of hydrated crystalline aluminosilicate of alkali and alkaline-earth metals.[33] Y zeolite displays the Faujasite (FAU) framework which has a 3D porous structure is known as one of the most accountable zeolites which has been employed for numerous research purposes so far.[33] Y zeolite possesses distinctive features like high surface area, large pore volume, high hydrothermal stability and biocompatibility which is advantageous for its use in catalysis, development of adsorbents, etc.[34–36] Elsewhere, in recent years, the inorganic spinel cobalt ferrite nanoparticles ($CoFe_2O_4$ NPs) with band gap energy 1.76 eV have grabbed much attention referred to their different properties such as coercivity, anisotropy, saturation, magnetization, etc.[37,38] Thereupon, these salient and applicable features make magnetic $CoFe_2O_4$ NPs suitable for several fields for instance drug delivery,[39] magnetic fluid hyperthermia,[40] microwave devices,[41] permanent magnets,[42] catalysis,[43] etc. The incorporation of various sorts of magnetic NPs over the surface of solid catalysts provides a high surface area to enhance the efficiency of the catalytic processes.[44] In this scientific research, for the first time, $CoFe_2O_4@Cr-MIL-101/Y$ zeolite as a novel magnetic catalyst nanocomposite was successfully fabricated using hydrothermal route and subsequently identified by several techniques including FTIR, XRD, FESEM, EDS, EDS dot-mapping, TEM, AFM, VSM, and BET analyses. The foregoing nanocomposite was then assessed for the sonodecomposition of the cationic and anionic organic dyes of methylene blue (MB), rhodamine B (RhB) and methyl orange (MO) in water solution by employing H_2O_2 (hydrogen peroxide) as the hydroxyl radicals (˙OH) source. However, as far as we know, there are no scientific researches reporting the sonodecomposition reactions of organic dye contaminants using the $CoFe_2O_4@Cr-MIL-101/Y$ zeolite catalyst nanocomposite in any previous study.

2. Experimental

2.1. Materials

Cobalt(II) nitrate hexahydrate ($Co(NO_3)_2 \cdot 6H_2O$, 98%), iron(III) nitrate nonahydrate ($Fe(NO_3)_3 \cdot 9H_2O$, 98%), terephthalic acid (H_2BDC, 98%), chromium(III) nitrate nonahydrate ($Cr(NO_3)_3 \cdot 9H_2O$, 99%), aluminum hydroxide ($Al(OH)_3$, 99%), sodium hydroxide (NaOH, 98%), hydrogen peroxide (H_2O_2, 30%), sodium silicate (Na_2SiO_3, 98%), ethanol (C_2H_5OH, 96%), dimethyl formamide (DMF, 99%), benzoquinone (BQ, 98%),

isopropyl alcohol (IPA, 99%), disodium ethylenediaminetetra-acetate (Na_2-EDTA, 99%), methyl orange (MO, $C_{14}H_{14}N_3NaO_3S$, 99%), rhodamine B (RhB, $C_{28}H_{31}ClN_2O_3$, 99%), and methylene blue (MB, $C_{16}H_{18}ClN_3S$, 99%) were all purchased from Alfa Aesar, Sigma-Aldrich and Merck companies.

2.2. Instrumentation

The morphological, structural and magnetic properties of the as-prepared catalysts were evaluated using different analytical instruments. In this respect, the Fourier transform infrared (FTIR) was applied on a Schimadzu system spectrophotometer 8400S utilizing KBr disks in the wavelength between 400–4000 cm^{-1}. The powder X-ray diffraction (XRD) patterns were surveyed by type XPERT Poro panalytical diffractometer along with Ni-filtered $CuK\alpha$ radiation at $\lambda = 1.5406$ Å (40 kV and 30 mA) and subsequently the related data were measured in the variation range of 2θ between 5° to 80° via a scanning speed of 2° min^{-1}. Elsewhere, a field emission scanning electron microscopy along with energy-dispersive X-ray spectroscopy (FESEM-EDS) and X-ray dot-mapping (MIRA3 TESCAN) via an operating voltage of 15 kV, were exerted to investigate the shape and crystalline size of the understudy catalysts. Meantime, the atomic force microscopy (AFM, Noncontact mode, Ara-AFM, model Full plus) was operated and experiments were implemented at 25 ± 1 °C. The transmission electron microscopy (TEM) analysis was utilized to characterize the particles size and morphology of the as-prepared catalyst nanocomposite with type Philips CM120 electron microscope at an 80 kV voltage. For the investigation of the magnetic properties of as-synthesized catalysts, a vibrating sample magnetometer (VSM, Magnetic Daghigh Kavir, MDKB model) was applied. The nitrogen Brunauer–Emmett–Teller (N_2-BET) with a PHSCHINA PHS1020 apparatus was used to study the specific surface area and pore size distributions of the catalysts at 77 K. Moreover, an ultrasonic device (Sonic 6MX; 100W output acoustic power and frequency of 37 kHz) was utilized to study all the sonodecomposition processes of organic dyes and the fabrication of the catalysts. A double-beam ultraviolet-visible (UV-Vis) spectrophotometer (Cary 100, Varian Company) was employed to evaluate the residual organic dyes concentrations from the supernatant aqueous solutions before and after the sonodecomposition reactions in the range wavelength between 200–800 nm.

2.3. Synthesis of Y type zeolite

Typically, an adequate amount of NaOH (10 g) was poured into the deionized water (10 mL). Afterwards, the value of $Al(OH)_3$ (9.75 g) was transferred into the NaOH solution and heated at temperature of 100 °C. Then, resultant suspension (10 g) was dissolved into the deionized water (61.2 mL) and subsequently NaOH (5.9 g) was added to this suspension until being dissolved to prepare the solution A. Meanwhile, Na_2SiO_3 (22 g) was gradually poured into the prepared solution containing NaOH (5.9 g) and deionized water (61.2 mL) until being dissolved to afford the solution B. The solution A was gently added to the solution B and acquired mixture was stirred for 40 min. The

molar composition of gel was $4.3Na_2O : Al_2O_3 : 10SiO_4 : 180H_2O$. The mixture was placed into a Teflon-lined stainless steel autoclave and heated at 90 °C for 8 h. The product was filtered and washed by distilled water until the neutral pH was achieved. Consequently, the final product was dried at 100 °C.[45]

2.4. Synthesis of Cr-MIL-101/Y zeolite

Firstly, as-prepared Y zeolite (0.2 g) was added into the deionized water (30 mL) and subsequently was dispersed under ultrasonic irradiation for 1 h. In the next step, the appropriate values of H_2BDC (0.5 g) and $Cr(NO_3)_3 \cdot 9H_2O$ (1.2 g) as the precursors were poured into the above specified solution and the solution was then rigorously agitated for 30 min at 25 ± 1 °C. Subsequently, the resultant suspension was transferred to a Teflon-lined stainless steel autoclave and heated at 200 °C overnight. The gained product was then left to be cooled down at 25 ± 1 °C. To achieve the extra purified sample, the resultant mixture was rinsed several times sequentially using the DMF and ethanol solvents to remove any possible impurities from the unreacted H_2BDC on its surface. Finally, the obtained sample was dried at 150 °C for 12 h to achieve the Cr-MIL-101/Y zeolite composite.

2.5. Synthesis of CoFe₂O₄@Cr-MIL-101/Y zeolite

A hydrothermal approach was employed to synthesize the magnetic $CoFe_2O_4@Cr$-MIL-101/Y zeolite catalyst nanocomposite as follows: the as-prepared Cr-MIL-101/Y composite (0.5 g) was appended into the deionized water (30 mL). Afterwards, the quantities of $Fe(NO_3)_3 \cdot 9H_2O$ (1.32 g) and $Co(NO_3)_2 \cdot 6H_2O$ (0.57 g) were added into the desired solution and subsequently stirred for 1 h at 25 ± 1 °C. Thereafter, as-prepared NaOH aqueous solution (1 mol L^{-1}) was gradually added to the above cited suspension to achieve pH of 11 while continuously stirring for 1 h. Then, the immobilization reaction was ceased and the mixture was calcined at 180 °C for 12 h. Ultimately, the attained precipitate was magnetically separated and thoroughly rinsed using the deionized water and ethanol for multiple times and dried at 25 ± 1 °C.

2.6. Sonodecomposition experiments

To scrutinize the sonocatalytic decomposition reactions of several organic cationic and anionic dyes including MB, RhB and MO over the desired catalysts from water solution, an ultrasonic device was applied. Typically, the amount of magnetic $CoFe_2O_4@Cr$-MIL-101/Y catalyst (0.5 g L^{-1}) was transferred into the MB aqueous solution (25 mg L^{-1}, 50 mL) and subsequently the resulting solution was shaken for 30 min in the darkness. This stirring step causes the formation an adsorption–desorption equilibrium among the catalyst surface and organic dye. In the next step, the reaction was accomplished using the H_2O_2 (40 mmol L^{-1}, 2 mL). After the desired time intervals, the reaction process was halted; the quantity of the aqueous solution (2 mL) was taken out and then the $CoFe_2O_4@Cr$-MIL-101/Y nanocomposite was separated from the supernatant solution using an external magnetic field. At the end, the transparent supernatant solution of the organic dye

was moved to the UV-Vis spectrophotometer instrument at λ_{max} of 663 nm to evaluate the residual MB dye. In addition, the influence of several independent factors such as initial dye concentration (25, 35, 45 and 55 mg L^{-1}), sonocatalyst kind (raw $CoFe_2O_4$, Y, Cr-MIL-101, Cr-MIL-101/Y and $CoFe_2O_4@Cr$-MIL-101/Y), sonocatalyst dosage (0.25, 0.5, 0.75 and 1 g L^{-1}), initial H_2O_2 concentration (5, 10, 20, 30, 40 and 50 mmol L^{-1}), and irradiation time (5, 10, 20, 30, 40, 50, and 60 min) over the sonodecomposition reactions of dyes were meticulously surveyed. Besides, to study the sonocatalytic performance of the $CoFe_2O_4@Cr$-MIL-101/Y nanocomposite to decompose and decontaminate other organic dyes namely RhB and MO from aqueous solution, the similar experimental conditions were employed and the acquired data were reported in the present research. The decomposition reaction efficiency% (DE%) was also investigated through the equation below (1):

$$DE\% = \left(1 - \frac{A_t}{A_0}\right) \times 100 = \left(1 - \frac{C_t}{C_0}\right) \times 100 \qquad (1)$$

In the aforementioned equation, A_0 and C_0, and also A_t and C_t parameters in mg L^{-1} are ascribed to the absorbance and concentration of decomposed MB dye at the initial and the specified reaction time interval in min, respectively.

3. Result and discussion

3.1. FTIR analysis

The Fourier transform infrared spectroscopy (FTIR) spectra of the as-prepared catalysts namely raw Y zeolite (Fig. 1a), Cr-MIL-101/Y (Fig. 1b), $CoFe_2O_4@Cr$-MIL-101/Y (Fig. 1c), raw $CoFe_2O_4$ (Fig. 1d), and raw Cr-MIL-101 (Fig. 1e) have been exhibited in Fig. 1. As demonstrated in Fig. 1a–c, the bands located at 459 cm^{-1} and 578 cm^{-1} are ascribed to the internal TO_4 (T = Al and/or Si elements) tetrahedral units and bending vibrations of the double six rings external linkage of Y zeolite, while the specified absorption bands at 719 cm^{-1} and 788 cm^{-1} can be assigned sequentially to the external linkage and vibrations O–T–O internal tetrahedral symmetrical stretching. Moreover, the observed bands near 1018 cm^{-1} and 1135 cm^{-1} are relevant to the O–Al–O and/or O–Si–O external connection and internal tetrahedral asymmetrical stretching vibrations of the Y zeolite. The bands at 1631 cm^{-1} and 3407 cm^{-1} can be attributed to the vibrations of hydroxyl groups and adsorbed H_2O molecules bonds including O–H bonding and H–O–H bending sequentially in the structure of Y zeolite. Additionally, the bands at about 1512 cm^{-1} and 1398 cm^{-1} which have been indicated from Fig. 1b and c, can be pertained to the C=C and carboxylate (O–C–O) bonds in H_2BDC which referred to the successful incorporation of Cr-MIL-101 in the structure of $CoFe_2O_4@Cr$-MIL-101/Y. On the other hand, the absorption bands affiliated to the M–O–Si and/or M–O–Al (M = Co and/or Fe elements) from the incorporation of $CoFe_2O_4$ on the Cr-MIL-101/Y framework expected in the range of 400 to 1000 cm^{-1}, were not illustrated because to the overlapping with the Y zeolite bands. The FTIR spectrum of the raw $CoFe_2O_4$ has been shown in Fig. 1d. The bands at about 3450 cm^{-1} and 1581 cm^{-1} are observed due to the adsorbed H_2O molecules on the surface of

CoFe$_2$O$_4$. The absorption bands between 400 cm^{-1} to 600 cm^{-1} were also recognized to the stretching vibrations of Co–O and Fe–O bonds. Also, Fig. 1e reveals FTIR spectrum of the raw Cr-MIL-101. The absorption bands in the range of 748 cm^{-1}, 881 cm^{-1}, 1016 cm^{-1}, 1161 cm^{-1}, and 1508 cm^{-1} are related to the C–H and C=C bonds, respectively. The absorption bands around 1400 cm^{-1} to 1662 cm^{-1} are assigned sequentially to the asymmetric stretching vibrations and carboxylate (COO) symmetric stretching vibration from the H$_2$BDC.

3.2. XRD analysis

Fig. 2 elucidates the X-ray diffraction (XRD) patterns of the raw Y zeolite (Fig. 2a), Cr-MIL-101/Y (Fig. 2b), CoFe$_2$O$_4$@Cr-MIL-101/Y (Fig. 2c), raw CoFe$_2$O$_4$ (Fig. 2d), and raw Cr-MIL-101 (Fig. 2e). As can be revealed from Fig. 2a–c, the several intense peaks belonged to the Y zeolite were determined at 2θ angles approximately 6.28°, 10.17°, 11.95°, 15.73°, 18.73°, 20.43°, 23.71°, 27.13°, and 32.54° sequentially recognized to the diffraction planes of (111), (220), (311), (331), (511), (440), (620), (533), and (733), which have been crystallized in the cubic structure with JCPDS card (41-0118). Besides, the main peaks of raw Cr-MIL-101 phase were observed at 2θ between 5° to 20° (Fig. 2d), which confirms the excellent crystalline framework of the fabricated sample. Also, by supporting of Cr-MIL-101 and CoFe$_2$O$_4$ subsequently over the Y zeolite surface to form the CoFe$_2$O$_4$@Cr-MIL-101/Y nanocomposite, no significant change was found in its crystalline structure. In this respect, the peaks attributed to the Cr-MIL-101 were demonstrated at scattering
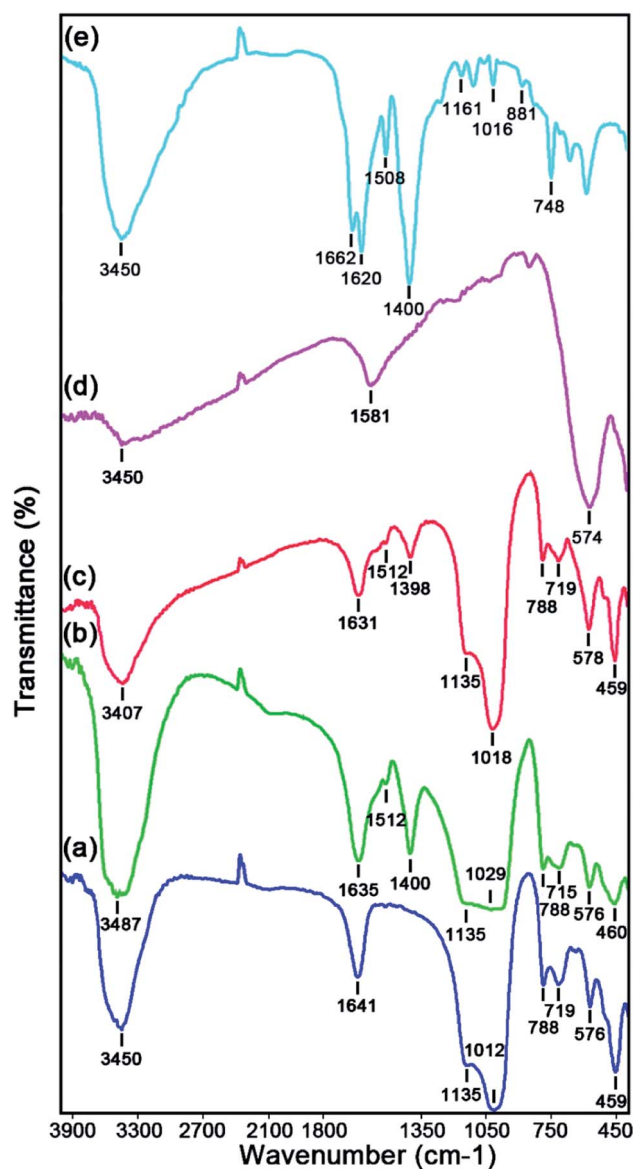

Fig. 1 FTIR spectra of the as-synthesized (a) raw Y zeolite, (b) Cr-MIL-101/Y, (c) CoFe$_2$O$_4$@Cr-MIL-101/Y, (d) raw CoFe$_2$O$_4$, and (e) raw Cr-MIL-101.
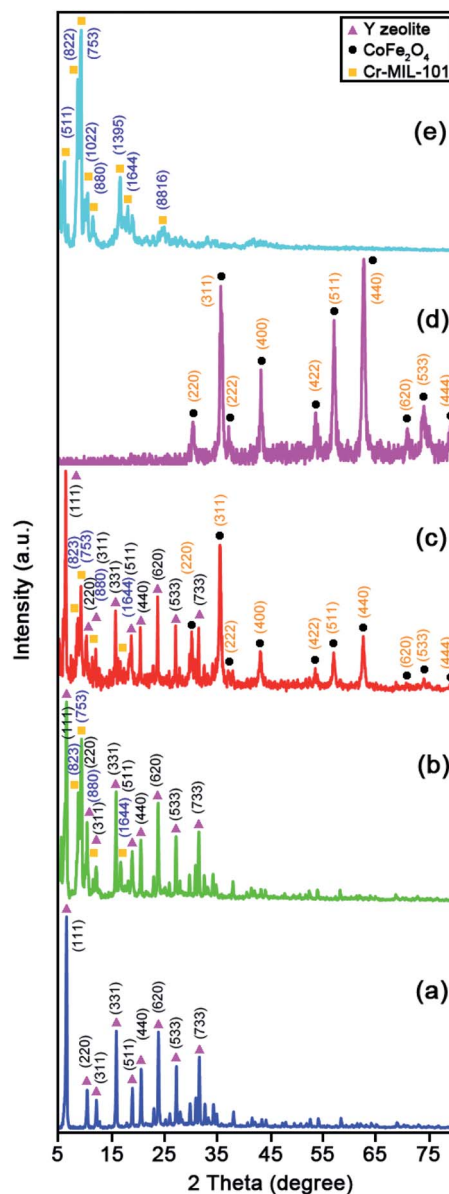

Fig. 2 XRD patterns of the as-synthesized (a) raw Y zeolite, (b) Cr-MIL-101/Y, (c) CoFe$_2$O$_4$@Cr-MIL-101/Y, (d) raw CoFe$_2$O$_4$, and (e) raw Cr-MIL-101.

angles (2θ) approximately 8.62, 9.18°, 11.45° and 16.60°, respectively. Moreover, several new peaks affiliated to the presence of $CoFe_2O_4$ throughout the fabrication process of the nanocomposite were located at 2θ of 30.34°, 35.67°, 37.12°, 43.29°, 53.65°, 57.20°, 62.82°, 71.25°, 74.23° and 78.97° corresponded to the (220), (311), (222), (400), (422), (511), (440), (620), (533), and (444) (JCPDS card: 01-1121). The average crystalline size (d_c) of the $CoFe_2O_4$ NPs over the Cr-MIL-101/Y was measured approximately 12 nm using the Debye–Scherrer eqn (2):

$$d_c = \frac{(0.9)\lambda}{\beta \cos \theta} \qquad (2)$$

herein, λ factor is the wavelength of X-ray, β shows the full width at half maximum (FWHM) of the desired diffraction pattern and θ is also recognized as the Bragg angle.

3.3. FESEM analysis

To survey the structure, morphology and size of the as-prepared samples, a field emission scanning electron microscopy (FESEM) analysis was applied. The FESEM images of the raw Y zeolite (Fig. 3a and b), Cr-MIL-101/Y (Fig. 3c and d), $CoFe_2O_4$@Cr-MIL-101/Y (Fig. 3e and f), raw $CoFe_2O_4$ (Fig. 3g), and raw Cr-MIL-101 (Fig. 3h and i) with different resolutions were all respectively indicated in Fig. 3. The cubic crystals of the Y zeolite, the octahedral framework of the Cr-MIL-101 and also the quasi-spherical shape of the $CoFe_2O_4$ were displayed from the FESEM images. Based on the attained data, it can be inferred that by supporting the Cr-MIL-101 and $CoFe_2O_4$ subsequently over the surface of the Y zeolite, its morphology and framework remained intact. Moreover, the average particles size of the $CoFe_2O_4$ NPs as the guest molecules within the $CoFe_2O_4$@Cr-MIL-101/Y catalyst were found to be about 12 nm.

3.4. EDS and EDS elemental dot-mapping analyses

The energy dispersive X-ray (EDS) was operated to fully clarify the elemental composition of the as-fabricated catalysts. Fig. 4 represents the EDS analysis of the raw Y zeolite (Fig. 4a), $CoFe_2O_4$@Cr-MIL-101/Y (Fig. 4b), raw $CoFe_2O_4$ (Fig. 4c), and raw Cr-MIL-101 (Fig. 4d), respectively. The acquired data from the analysis elucidates the existence of the four main elements of Si, O, Al and Na in all of the samples including raw Y zeolite and $CoFe_2O_4$@Cr-MIL-101/Y. Also, Fig. 4b displays the presence of a series of other elements such as Co, Fe and O related to the $CoFe_2O_4$ NPs, and plus Cr, C and O corresponded to the Cr-MIL-101 within the framework of the $CoFe_2O_4$@Cr-MIL-101/Y ternary nanocomposite, which affirms the formation of the $CoFe_2O_4$ and Cr-MIL-101 over the Y zeolite (see Table 1). Also, as can be seen from Fig. 4b and d, composition analyses of the C

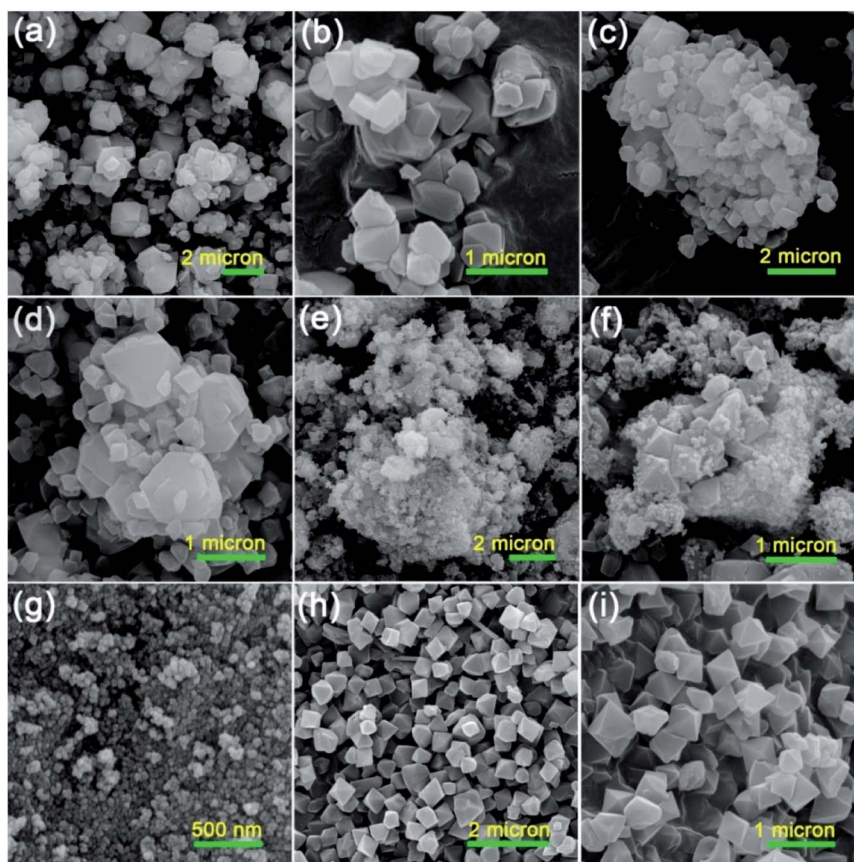Fig. 3 FESEM images of the as-synthesized (a and b) raw Y zeolite, (c and d) Cr-MIL-101/Y, (e and f) $CoFe_2O_4$@Cr-MIL-101/Y, (g) raw $CoFe_2O_4$, (h and i) raw Cr-MIL-101 with different resolutions.

and O elements clearly approved the presence of carboxylate within the Cr-MIL-101 frameworks. Further, the FESEM image affiliated to the EDS elemental dot-mappings of the $CoFe_2O_4$@Cr-MIL-101/Y were depicted in Fig. 4e. Evaluating the elemental mappings analysis represented in Fig. 4e, the uniform distribution of Si, O, Al, Na, Co, Fe, Cr and C elements on the nanocomposite is clearly verified.

3.5. TEM analysis

The TEM analysis was applied to further warrant the particle size and morphology of the as-prepared $CoFe_2O_4$@Cr-MIL-101/Y nanocomposite. The TEM images of $CoFe_2O_4$@Cr-MIL-101/Y with different resolutions are shown in Fig. 5a–c. Regarding the TEM images, it can be deduced that the both Cr-MIL-101

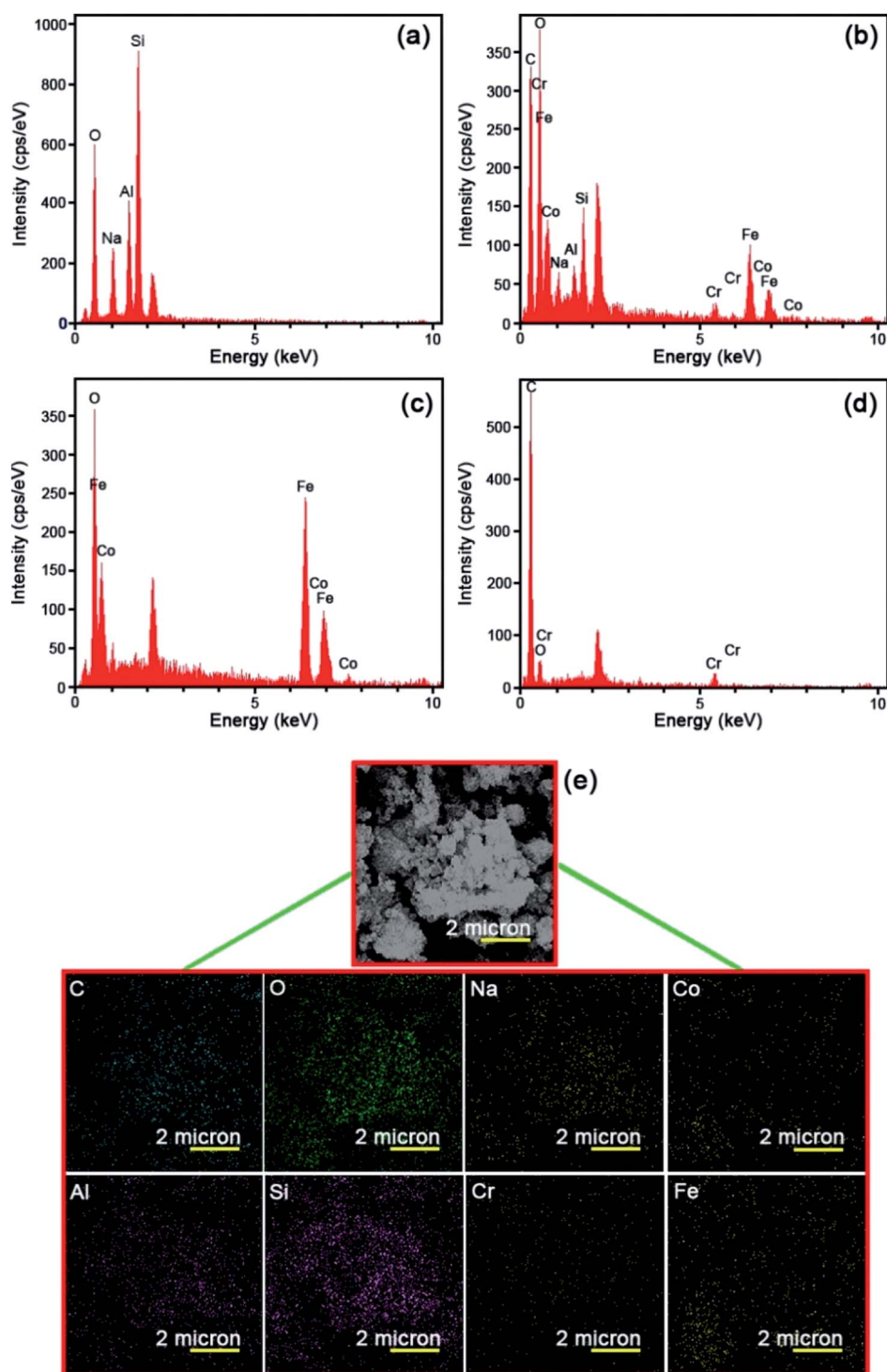Fig. 4 EDS analyses of the as-synthesized (a) raw Y zeolite, (b) $CoFe_2O_4$@Cr-MIL-101/Y, (c) raw $CoFe_2O_4$, (d) raw Cr-MIL-101, and (e) FESEM image affiliated to the EDS dot-mappings of the as-synthesized $CoFe_2O_4$@Cr-MIL-101/Y.

Table 1 The quantitative results of the elemental composition of the as-synthesized CoFe$_2$O$_4$@Cr-MIL-101/Y zeolite catalyst nanocomposite

Element type	Line	Weight%	Atomic%
C	Kα	47.77	61.25
O	Kα	33.43	32.17
Na	Kα	1.51	1.01
Al	Kα	0.97	0.55
Si	Kα	2.03	1.11
Cr	Kα	0.88	0.26
Fe	Kα	8.81	2.43
Co	Kα	4.60	1.20

and CoFe$_2$O$_4$ NPs as the guest molecules were successfully incorporated over the Y zeolite structure. The mediocre particle diameter about 12 nm and plus the narrow particle size distribution between 8 to 16 nm were clearly identified using the TEM images. The abovementioned results were in good agreement with the mediocre particle diameter attained *via* the FESEM and XRD analyses.

3.6. AFM analysis

The atomic force microscopy (AFM) is recognized as a suitable analytical method to study several important properties of the as-obtained catalysts such as surface roughness, size and topography. Fig. S1† represents AFM 2-dimensional (2D) and 3-dimensional (3D) images ascribed to the raw Y zeolite (Fig. S1a and b†), Cr-MIL-101/Y (Fig. S1c and d†) and CoFe$_2$O$_4$@Cr-MIL-101/Y (Fig. S1e and f†), respectively. By comparing the images, it is brightly indicated that the surface of the Y zeolite was mainly covered *via* the Cr-MIL-101 and CoFe$_2$O$_4$ NPs, which refers to
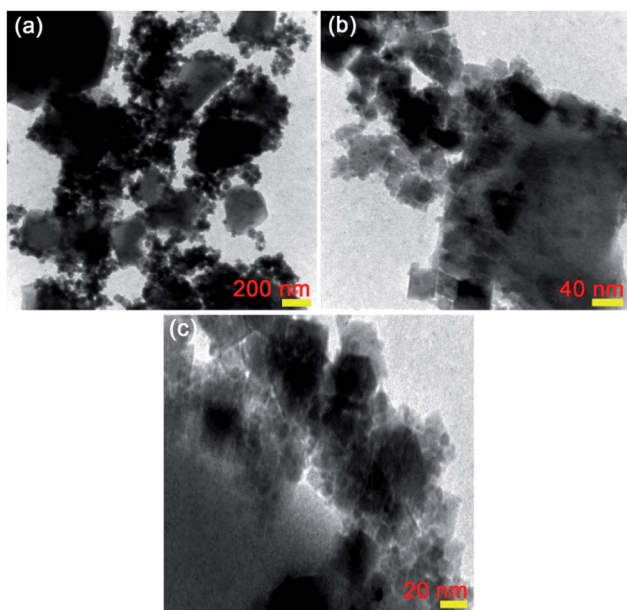
the successful synthesis of the aforementioned guest molecules within the host framework. Besides, mean size of the composed CoFe$_2$O$_4$ NPs in the CoFe$_2$O$_4$@Cr-MIL-101/Y catalyst were approximately about 12.8 nm, which acquired data from this analysis are in good consistency with the FESEM, TEM and XRD.

3.7. VSM analysis

The vibrating sample magnetometer (VSM) analysis was utilized to thoroughly investigate the magnetic properties of the as-prepared samples at 25 ± 1 °C. Fig. 6 reveals the hysteresis loops of the raw CoFe$_2$O$_4$ NPs (Fig. 6a) and CoFe$_2$O$_4$@Cr-MIL-101/Y (Fig. 6b). Both raw CoFe$_2$O$_4$ NPs and CoFe$_2$O$_4$@Cr-MIL-101/Y illustrate the ferromagnetic features due to the existence of three parameters namely coercive force (H_c), remnant magnetization (M_r) and saturation magnetization (M_s). In this respect, the values of the H_c, M_r and M_s parameters of the raw CoFe$_2$O$_4$ NPs were determined approximately at about 1500 Oe, 33.94 emu g^{-1} and 63.46 emu g^{-1}, whereas by supporting of the CoFe$_2$O$_4$ NPs on the surface of the Cr-MIL-101/Y, the abovementioned values decreased to 2500 Oe, 15.10 emu g^{-1} and 26.10 emu g^{-1}, respectively. Consequently, it is deduced that the CoFe$_2$O$_4$@Cr-MIL-101/Y nanocomposite can be separated from the reaction solution in the shortest possible time using a simple external magnetic field.

3.8. BET analysis

To meticulously unveil the structural outstanding of the as-prepared catalysts, BET analysis was utilized. Fig. 7 demonstrates the N$_2$ adsorption–desorption isotherms and pore size distributions of raw Y zeolite (Fig. 7a) and CoFe$_2$O$_4$@Cr-MIL-101/Y (Fig. 7b), respectively. Pursuant to the acquired plot of isotherms of the understudy catalysts, it is obviously known that these plots can be assorted to type-IV isotherm with a H3 hysteresis loops (as per IUPAC recommendation), which affirmed the presence of mesoporous structure of the catalysts. The values of BET specific surface area for raw Y zeolite and CoFe$_2$O$_4$@Cr-MIL-101/Y were also measured about 494 and 222 m^2 g^{-1} respectively and reflected in Table 2. As can be seen in

Fig. 5 TEM images of the as-synthesized (a–c) CoFe$_2$O$_4$@Cr-MIL-101/Y with different resolutions.
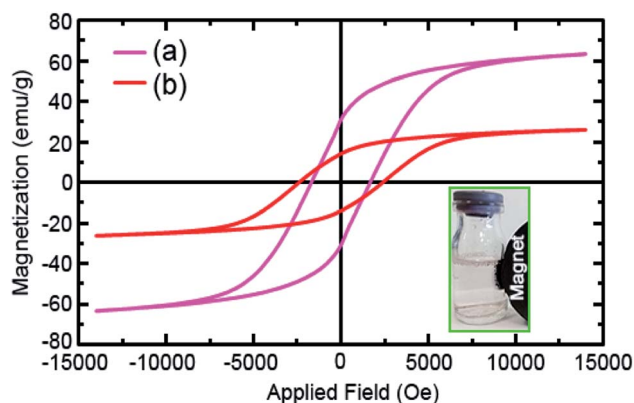
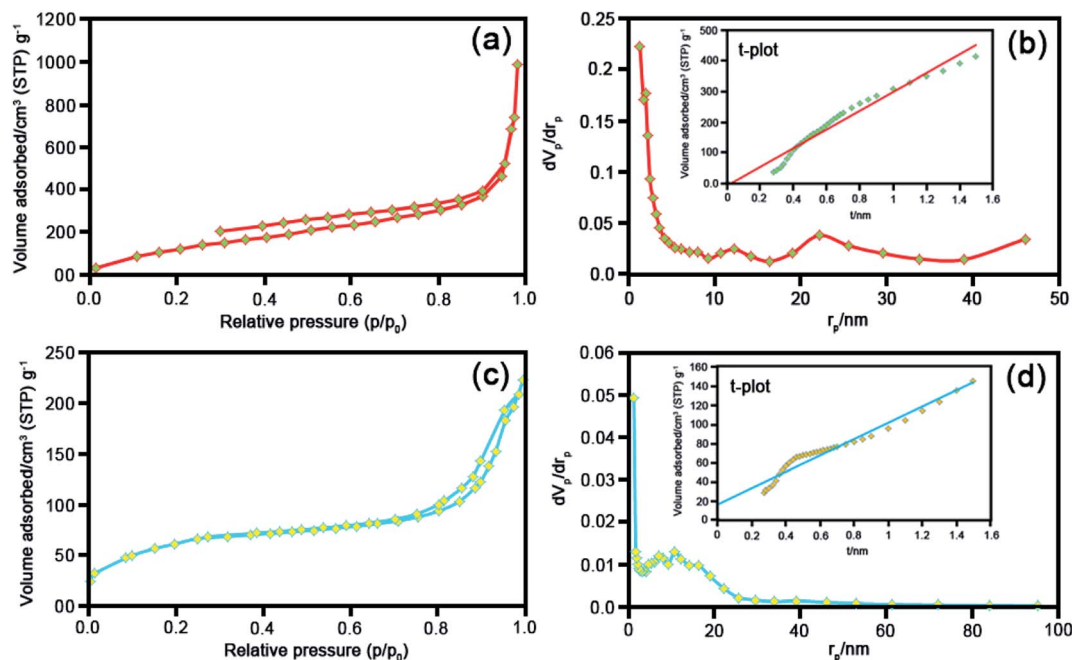**Fig. 6** VSM curves of the as-synthesized (a) raw CoFe$_2$O$_4$ and (b) CoFe$_2$O$_4$@Cr-MIL-101/Y.

Fig. 7 BET analyses, BJH and *t* plots of the as-synthesized (a) and (b) raw Y zeolite, (c) and (d) CoFe$_2$O$_4$@Cr-MIL-101/Y.

Table 2, the acquired specific surface area, pore size distributions, V_{me} and V_{mi} of CoFe$_2$O$_4$@Cr-MIL-101/Y decreases in comparison with raw Y zeolite, which confirms the formation of the Cr-MIL-101 and CoFe$_2$O$_4$ on the Y zeolite framework.

3.9. Sonodecomposition processes investigation

3.9.1. The influence of the irradiation time. The irradiation time is an effective factor for the investigation of the cationic and anionic dyes sonodecomposition reactions using the CoFe$_2$O$_4$@Cr-MIL-101/Y zeolite catalyst. To meticulously evaluate these reactions, a period of time intervals was considered and the gained data studied to survey for all of the sonocatalytic experiments. Investigating the acquired results from the experiments clearly approved the remarkable dependency between the decomposition percentage and different reaction times. Thus, the sonodecomposition processes were done using the determined absorption bands ascribed to the MB organic dye at λ_{max} about 663 nm. At first, the intended amount of CoFe$_2$O$_4$@Cr-MIL-101/Y zeolite catalyst (0.5 g L^{-1}) was transferred into the MB aqueous media (50 mL, 25 mg L^{-1}) and the resulted suspension was exposed to the US irradiation along with H$_2$O$_2$ (40 mmol L^{-1}). As can be observed in Fig. 8a and b, the tangible differences between the gained UV-Vis analysis

spectra of the MB aqueous media in the reaction with the CoFe$_2$O$_4$@Cr-MIL-101/Y zeolite catalyst indicates the prominent role of the shaking time. Based on the observations on the attained spectra it becomes crystal clear that the stringency of the punctuated peak assigned to MB (emerged at 663 nm) is directly affected by the time intervals. As time goes on, the intensity of the specified peak diminishes ceaselessly till the point of 60 min at which it becomes almost hard to be spotted which is connoting the high yield decomposition of MB (98.9%). According to the implemented sonocatalytic experiments and evaluated results on decomposition of MB dye, the particular visible light sono decomposition role of the CoFe$_2$-O$_4$@Cr-MIL-101/Y zeolite nanocomposite is vividly confirmed.

As it has been displayed in Fig. 8c, plotting ln initial dye concentration *versus* contact time (min) results in some curves which are of great significance for the investigation of the sonodecomposition reaction kinetics. Elsewhere, the decomposition rate constant symbolized as k (min^{-1}), was calculated using the first order equation of

$$\ln(C_o/C_t) = kt. \qquad (3)$$

In the represented equation, C_o is defined as the initial concentration of the understudy dye, C_t represents the dye

Table 2 The acquired data from the N$_2$-BET, BJH and *t* plots corresponded to the as-synthesized catalysts at 77 K

Sample	a_s, BET [m^2 g^{-1}]	V_{me} [cm^3(STP) g^{-1}]	V_{mi} [cm^3(STP) g^{-1}]	Total pore volume [cm^3 g^{-1}]	Average pore diameter [nm]
Y zeolite	494	113	0.10	1.50	12.44
CoFe$_2$O$_4$@Cr-MIL-101/Y	222	51.06	0.02	0.34	6.11

concentration at time interval of t and k symbolizes the decomposition rate constant. Meanwhile, the half-life ($t_{1/2}$) amount was also computed employing the equation of

$$t_{1/2} = \ln(2)/k. \qquad (4)$$

To specify the mentioned adsorption kinetics, the value of 0.5 g L^{-1} of CoFe$_2$O$_4$@Cr-MIL-101/Y zeolite was introduced to several containers each comprising 25 mg L^{-1} of the considered dye at certain time periods and the subsequent relevant outcomes were demonstrated in Table 3. To provide an overview on the potentials and workability of each participant component in the decomposition reaction of MB dye, several systems of US, US/ H$_2$O$_2$, US/H$_2$O$_2$/Y, US/H$_2$O$_2$/Cr-MIL-101, US/H$_2$O$_2$/CoFe$_2$O$_4$, US/ CoFe$_2$O$_4$@Y, US/H$_2$O$_2$/Cr-MIL-101/Y, H$_2$O$_2$/CoFe$_2$O$_4$@Cr-MIL-101/Y, US/CoFe$_2$O$_4$@Cr-MIL-101/Y, and US/H$_2$O$_2$/CoFe$_2$O$_4$@Cr-MIL-101/Y were designed and employed as the relevant results have been represented in Fig. 8a–c. In addition, the value of 25 mg L^{-1} as the initial concentration of MB dye was appointed for all of those specified experiments. In brief, the collected information from the implemented experiments revealed a decomposition sequence consisting of US/H$_2$O$_2$/CoFe$_2$O$_4$@Cr-MIL-101/Y (98.9%) > US/H$_2$O$_2$/Cr-MIL-101/Y (54.5%) > US/

CoFe$_2$O$_4$@Cr-MIL-101/Y (48.1%) > US/H$_2$O$_2$/CoFe$_2$O$_4$ (41.5%) > US/CoFe$_2$O$_4$@Y (37.56%) > H$_2$O$_2$/CoFe$_2$O$_4$@Cr-MIL-101/Y (34.38%) > US/H$_2$O$_2$/Cr-MIL-101 (23%) > US/H$_2$O$_2$/Y (19.1%) > US/H$_2$O$_2$ (9.55%) > US (only), with respective constant values of 0.0675, 0.0114, 0.0109, 0.0083, 0.0072, 0.0071, 0.0042, 0.0034, 0.0016, and 0.0000 min^{-1} (see Table 3). Pursuant to the analysis outcomes, US/H$_2$O$_2$/CoFe$_2$O$_4$@Cr-MIL-101/Y was recognized as the most operative system for the decomposition of MB which is related to the impeding of the electron–hole incorporation by the linkage among Y zeolite, Cr-MIL-101 and CoFe$_2$O$_4$. The obtained data illuminates that reaction components including CoFe$_2$O$_4$@Cr-MIL-101/Y, US and H$_2$O$_2$ undoubtedly exhibit great performance for the decomposition process of MB dye in aqueous solutions. Additionally, applying US along with H$_2$O$_2$ method, intensifies the emission of hydroxyl radicals leading to the effectively much higher decomposition efficiency of the desired dye. Also, this decomposition efficiency can be explained as the generation of more oxidizing radicals in the presence of a higher concentration of H$_2$O$_2$. On the other hand, it should be noted that the sonocatalytic decomposition process in the absence of H$_2$O$_2$ (here focusing on US/CoFe$_2$O$_4$@Cr-MIL-101/Y) occurs most probably via the formation of ˙OH radicals
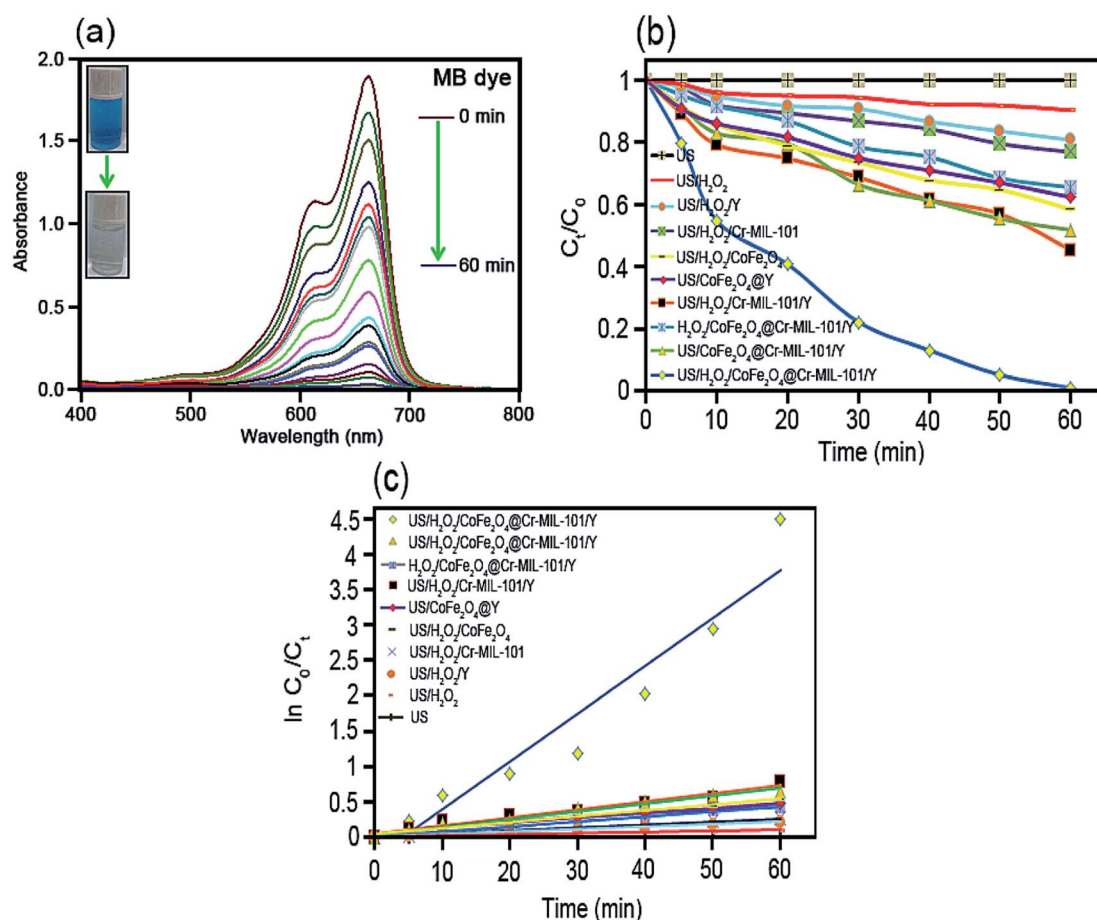
Fig. 8 UV-Vis absorption spectra of the sonodecomposition process of MB dye over the CoFe$_2$O$_4$@Cr-MIL-101/Y catalyst nanocomposite as a function of the irradiation time (a and b), the first order kinetic plot (ln(C_0/C_t)) against the irradiation time (c) (optimized experimental conditions; [MB dye]$_o$: 25 mg L^{-1} (50 mL), [H$_2$O$_2$]: 40 mmol L^{-1} (2 mL), [catalyst dosage]: 0.5 g L^{-1}, pH: 7 and temperature: 25 ± 1 °C).

using the degradation of H_2O molecules. In contrast, when H_2O_2 as oxidizing agent was appended to the understudy systems, the generation of ˙OH radicals were considerably accelerated related to the degradation of H_2O_2 *via* the generated electrons on the catalysts surface. According to what specified above, it is deduced that US/H_2O_2/CoFe$_2O_4$@Cr-MIL-101/Y, US/CoFe$_2O_4$@Cr-MIL-101/Y and H_2O_2/CoFe$_2O_4$@Cr-MIL-101/Y systems have the same mechanism for the degradation of dyes.

3.9.2. The influence of the organic dye type. To survey the potential of the sonodecomposition processes using the CoFe$_2O_4$@Cr-MIL-101/Y zeolite catalyst, the reactions were performed in the presence of RhB and MO dyes from water solution. According to the acquired data from Fig. 9a–c, the sonodecomposition yields of MO and RhB dyes at λ_{max} about 554 nm and 463 nm were determined more than 94% and 82% at time intervals of 60 min and 70 min, respectively. Consequently, the results showed that several factors for example electric charges, molecule sizes, chemical compositions and so on, can cause differences in the potentials and applications of the as-fabricated CoFe$_2O_4$@Cr-MIL-101/Y zeolite catalyst in the sonodecomposition reactions.

3.9.3. The influence of the initial dye concentration. To investigate and characterize the performance of the initial MB dye concentration and its pursuant influence on the sonodecomposition process is of great significance. It provides an evaluating ground which elucidates the operable strength of a definite value of the CoFe$_2O_4$@Cr-MIL-101/Y zeolite catalyst nanocomposite toward the continuous increase in the concentration of the organic dye. In this regard, a series of experiments were meticulously designed and implemented at which the value of CoFe$_2O_4$@Cr-MIL-101/Y zeolite remained unchanged while the concentration of the organic dye enhanced consecutively. From the Fig. S2,† it can be obviously comprehended that as the concentration of the dye rises from 25 to 55 mg L^{-1}, the decomposition efficiency drops tangibly from 98.9% to 45.6%. This observed phenomenon is attributed to unbalanced values of the synthesized nanocomposite against the increased concentration of dye molecules. Hence, it is inferred that the higher the concentration of the target dye molecules, the more the number of occupied active sites on the nanocomposite catalyst. In addition to what illustrated above, it can be

meaningfully concluded that the reduced decomposition efficiency is dependent to the sudden and consecutive increase in dosage of the organic dye and plus the constant quantities of the synthesized nanocomposite, H_2O_2 and its related to ˙OH (hydroxyl radicals) at definite irradiation time. Ultimately, the lack of proportionate recipient sites along with the loss of the hydroxyl radicals originated from H_2O_2 negatively affected the decomposition process.

3.9.4. The influence of the H_2O_2 concentration. Hydrogen peroxide and its subsequent affiliated hydroxyl radicals perform a particular role in the entire decomposition process which should not be superficially handled. From this point of view, to explore all aspects of the reaction and to pick up the most relevant concentration of hydrogen peroxide as the main spring of hydroxyl radicals is of undeniable importance. According to that, six separated experiments were precisely designed and pursuantly performed to find out the optimized dosage of the hydrogen peroxide ranging from 5–50 mmol L^{-1} prior to the decomposition of MB dye in CoFe$_2O_4$@Cr-MIL-101/Y nanocomposite catalyst. Looking crossly to the results as have been represented in Fig. S3,† it is observed that in concentrations of 5 and 10 mmol L^{-1} of H_2O_2, the decomposition efficiencies of 54.5% and 69.7% in 60 min were respectively attained. Additionally, further increase in concentration of H_2O_2 (20 to 40 mmol L^{-1}) led to a considerable enhancement of the decomposition efficiencies from 81.1% to 98.9% in 60 min respectively. This phenomenon affirms the undeniable coherency between the dosage of hydrogen peroxide and its subsequent off shoot hydroxyl radicals with the final decomposition efficiency. On the other hand, further intensification in concentration of hydrogen peroxide beyond 40 mmol L^{-1} caused a consecutive decreasing order which is referred to the additional amounts of H_2O_2 functioning as ˙OH scavenger to generate perhydroxyl (HOO˙) radicals with lower oxidation sufficiency. Thereupon, the concentration of 40 mmol L^{-1} was considered and applied as the optimized value of H_2O_2 for pursuant decomposition reactions.

3.9.5. The influence of the catalyst dosage. It has always been an ideal horizon to use the least amount possible of an adsorbent to reach the highest efficiency of adsorption or decomposition. From this point of view, to indicate the most

Table 3 The attained data for the MB sonodecomposition reactions *via* different processes (optimized experimental conditions; irradiation time: 60 min, [MB]$_o$: 25 mg L^{-1} (50 mL), [H_2O_2]: 40 mmol L^{-1} (2 mL), [catalyst dosage]: 0.5 g L^{-1}, pH: 7 and temperature: 25 ± 1 °C)

Process type	Rate constant (k, min^{-1})	Half-life ($t_{1/2}$, min)	Kinetic equation [$\ln C_o/C_t = at + b$]
US only	0.0000	0.0000	$y = 0.0000$
US/H_2O_2	0.0016	433.1250	$y = 0.0016x + 0.0112$
US/H_2O_2/Y	0.0034	203.8235	$y = 0.0034x + 0.0076$
US/H_2O_2/Cr-MIL-101	0.0042	165.0000	$y = 0.0042x + 0.0145$
US/H_2O_2/CoFe$_2O_4$	0.0071	97.6056	$y = 0.0071x + 0.0090$
US/CoFe$_2O_4$@Y	0.0072	96.2500	$y = 0.0072x + 0.0486$
US/H_2O_2/Cr-MIL-101/Y	0.0114	60.7894	$y = 0.0114x + 0.0525$
H_2O_2/CoFe$_2O_4$@Cr-MIL-101/Y	0.0083	83.4939	$y = 0.0083x + 0.0451$
US/CoFe$_2O_4$@Cr-MIL-101/Y	0.0109	63.5779	$y = 0.0109x + 0.0378$
US/H_2O_2/CoFe$_2O_4$@Cr-MIL-101/Y	0.0675	10.2666	$y = 0.0675x - 0.2700$

applying concentration of the sonocatalyst for the decomposition of considered organic dye, multiple experiments each representing different values of $CoFe_2O_4$@Cr-MIL-101/Y zeolite (ranging from 0.25 to 1 g L^{-1}) were defined and carried out and the affiliated results were demonstrated in Fig. S4.† It is also emphasized that the quantities of other participant species of the reaction including the understudy hydrogen peroxide (40 mmol L^{-1}) and organic dye (25 mg L^{-1}) kept unchanged throughout the assigned experiments. In consequence, as the concentration of the nanocomposite sonocatalyst was enhanced, the better results for the decomposition process were recorded. Nevertheless, this gradual ascendant procedure was substituted by a diminution sequence at concentrations higher than 0.5 g L^{-1}. As a matter of fact, it is inferred that continuous increase in catalyst dosage provides much more active sites accompanied by hydroxyl radicals on the $CoFe_2O_4$@Cr-MIL-101/Y zeolite which counts as the major reason for the increase of the decomposition efficiency. Moreover, the reported incessant decrease after the concentration of 0.5 g L^{-1} is assigned to the aggregation of the present nanoparticles related to the sonocatalyst as it is likely for them to detrimentally affect the decomposition process by reducing the number and dispensation of the active sites and further suppressing the ultrasonic

waves transmittal into the working solution which weakens the ultrasonic scattering procedure. According to what explained above, the concentration of 0.5 g L^{-1} was assigned as the optimized value of the synthesized sonocatalyst for the ulterior designed experiments.

3.9.6. **The influence of the scavenger type.** To provide an explicit perception of the influential species and to indicate their function as practical active oxidants through the decomposition reactions, several experiments were organized and sequentially implemented. In this regard, delving into Fig. S5† leads to a substantial deduction. It clarifies when 5 mmol L^{-1} of isopropyl alcohol (IPA) performing as 'OH scavenger was poured into the solution comprising 0.5 g L^{-1} of the catalyst nanocomposite and 25 mg L^{-1} of MB, the decomposition efficiency phenomenally dropped to 32% after 60 min of irradiation. Based on the described observation, the essentiality of existence and the irrefutable role of hydroxyl radicals as oxidants in the sonocatalytic process can be strongly emphasized. On the other hand, the addition of disodium ethylenediaminetetraacetate (Na_2-EDTA) and benzoquinone (BQ) as hole (h^+) and superoxide ($'O_2^-$) scavengers to the above cited solution caused an inconspicuous decrease in the decomposition efficiency of MB dye. Considering the gathered results from
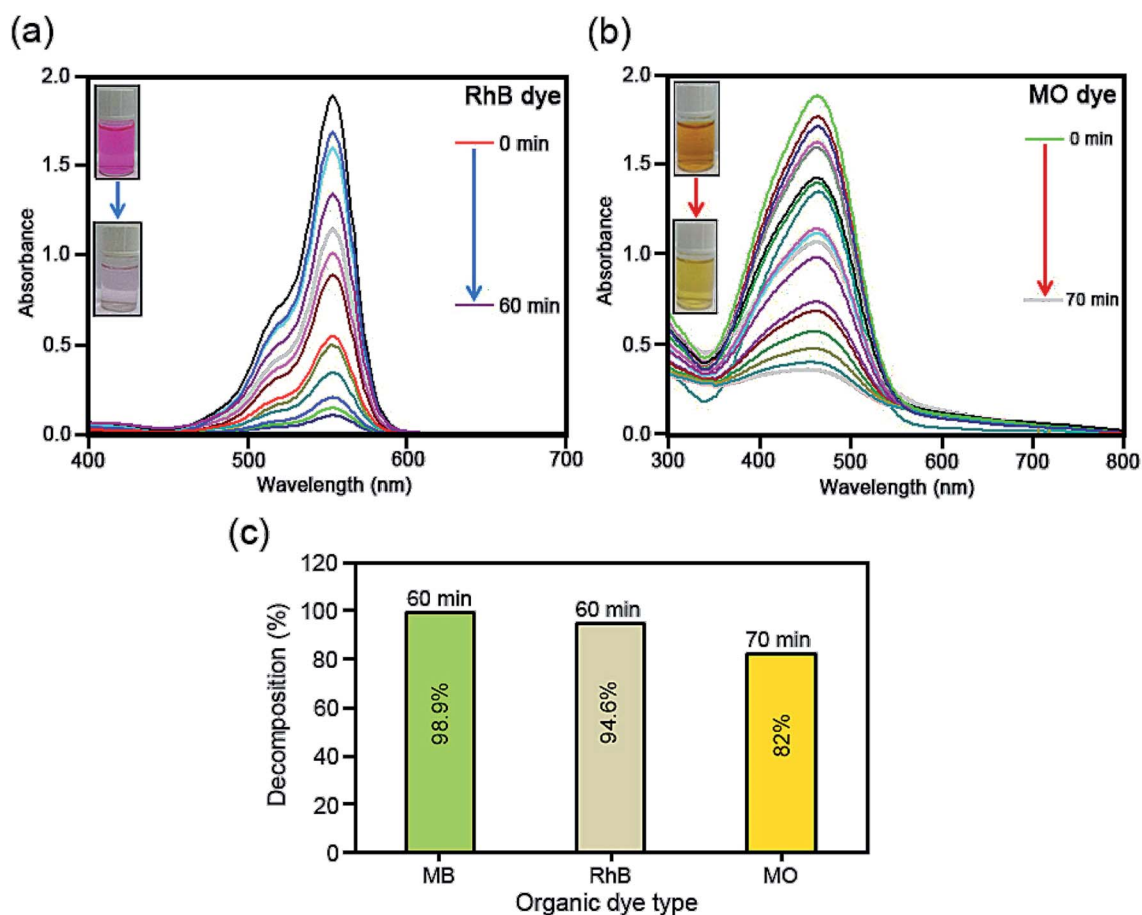

Fig. 9 UV-Vis absorption spectra of (a) RhB and (b) MO. (c) Decomposition efficiency% of MO and RhB dyes as a function of the irradiation time over the $CoFe_2O_4$@Cr-MIL-101/Y catalyst nanocomposite (optimized experimental conditions; $[dye]_o$: 25 mg L^{-1} (50 mL), $[H_2O_2]$: 40 mmol L^{-1} (2 mL), [catalyst dosage]: 0.5 g L^{-1}, pH: 7, and temperature: 25 ± 1 °C).
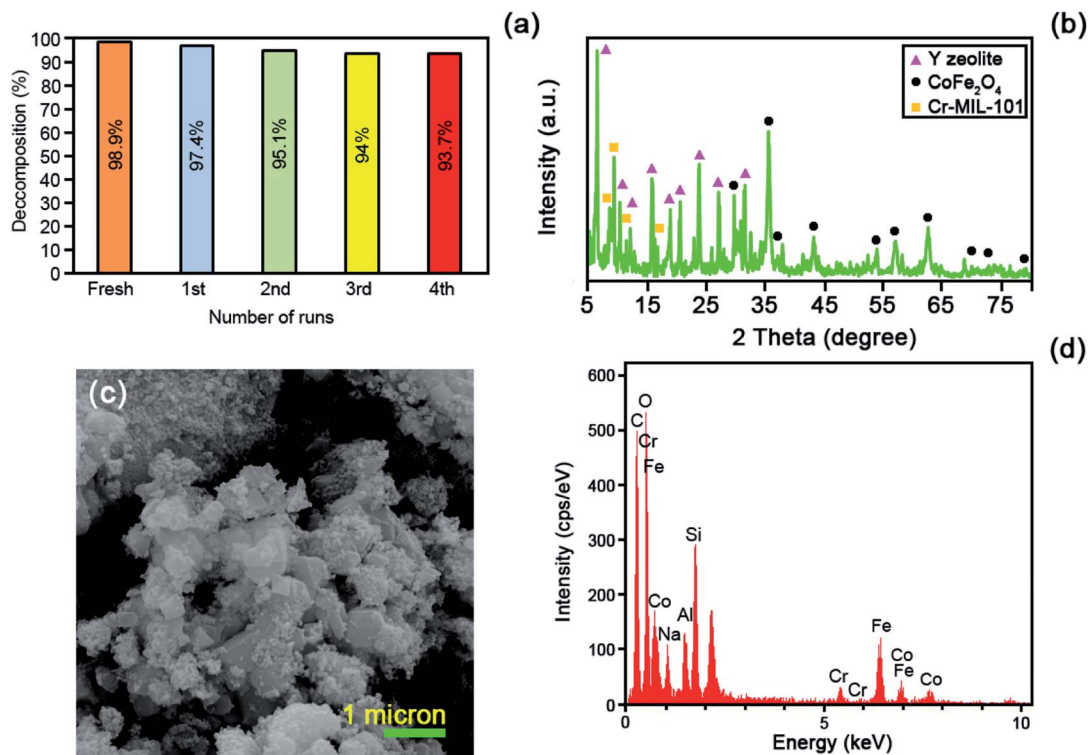
Fig. 10 (a) The regeneration plot, (b) XRD (c) FESEM, and (d) EDS analyses of the recovered $CoFe_2O_4/Y@Cr$-MIL-101 on the sonodecomposition process of MB after four runs (optimized experimental conditions; irradiation time: 60 min, $[MB]_o$: 25 mg L^{-1} (50 mL), $[H_2O_2]$: 40 mmol L^{-1} (2 mL), [catalyst dosage]: 0.5 g L^{-1}, pH: 7 and temperature: $25 \pm 1\,°C$).

those above specified experiments, it is perceived that the noted holes and superoxides display auxiliary roles either as ˙OH origins or oxidizing agents.

3.9.7. Regeneration and stability of the $CoFe_2O_4$@Cr-MIL-101/Y zeolite. In order to investigate the applicable potentials and the regeneration of the synthesized sonocatalyst, the spent $CoFe_2O_4$@Cr-MIL-101/Y zeolite was submerged in a solution of ethanol–deionized water. The implemented washing procedure leads to the segregation of the MB molecules from the $CoFe_2$-O_4@Cr-MIL-101/Y zeolite sonocatalyst nanocomposite. Afterwards, the recovered sonocatalyst was dried and repeatedly exerted for some several continual decomposition runs. In fact, a negligible decline in the regeneration of $CoFe_2O_4$@Cr-MIL-

101/Y was spotted after the first run. However, the high decomposition efficiency results recorded for those assigned frequent runs verify the significant potentials and reliability of the synthesized catalyst nanocomposite in diverse decomposition runs. As it can be observed in Fig. 10a, the regeneration phase was renewed four times and applying the regenerated catalyst nanocomposite led to the decomposition efficiencies of higher than 93% for all of those cited runs. Additionally, XRD, FESEM and EDS techniques were all utilized to provide a better understanding of the regenerated and fresh $CoFe_2O_4$@Cr-MIL-101/Y and plus to identify any possible characteristic conversion or disfiguration. Fig. 10b–d display the outcomes gathered from those above specified techniques. The XRD results showed

Table 4 A comparison between the $CoFe_2O_4$@Cr-MIL-101/Y and several reported catalysts

No	Catalyst type	Irradiation type	Dye type	$[H_2O_2]_o$ (mmol L^{-1})	$[Dye]_o$ (mg L^{-1})	[Catalyst] (g L^{-1})	Time (min)	Eff.%	Ref.
1	Cr-MIL-101@NiO/13X	Ultrasonic	MB	40	25	0.5	80	97.2	26
2	Cr-MIL-101@NiO/13X	Ultrasonic	RhB	40	25	0.5	80	94.3	26
3	TiO_2@CNTs/AgNPs/C10	Visible light	MB	0.782 mol L^{-1}	20	0.5	120	100	46
4	Fe_3O_4	Ultrasonic	RhB	40	0.02	0.5	60	90	47
5	Fe_3O_4/Al-B	Visible light	RhB	50	40	0.5	300	95	48
6	SCN/$CoFe_2O_4$	Ultrasonic	MB	4 vol%	25	1	20	83	49
7	SCN/$CoFe_2O_4$	Ultrasonic	RhB	4 vol%	25	1	20	20	49
8	$CoFe_2O_4$@Cr-MIL-101/Y	Ultrasonic	MB	40	25	0.5	60	98.9	This work
9	$CoFe_2O_4$@Cr-MIL-101/Y	Ultrasonic	RhB	40	25	0.5	60	94.6	This work

no considerable variation between the fresh and the regenerated CoFe$_2$O$_4$@Cr-MIL-101/Y after the fourth run (Fig. 10b). Besides, the FESEM technique (Fig. 10c) proved that there was no sensible transfiguration or deleterious alteration in the framework of CoFe$_2$O$_4$@Cr-MIL-101/Y after the fourth run compared to the fresh nanocomposite catalyst. Elsewhere, as it has been depicted in Fig. 10d, the EDS analysis exposed some substantial characteristic peaks of Si, O, Al, Na, Co, Fe, Cr and C affiliated to the regenerated CoFe$_2$O$_4$@Cr-MIL-101/Y after the fourth run of handling.

3.9.8. Comparison of CoFe$_2$O$_4$@Cr-MIL-101/Y zeolite with other research works. To precisely appraise the performance of the as-fabricated CoFe$_2$O$_4$@Cr-MIL-101/Y zeolite, the decomposition efficiency of this nanocomposite against several other catalysts was compared (see Table 4).[26,46–49] The represented results from several designed experiments and also characterization studies along with the comparison with other research works in the same field, all confirm the superiority of the newly introduced catalyst nanocomposite *versus* the others.

3.9.9. Plausible mechanism of the dyes sonodecomposition process. It is explicitly known that the high temperature and pressure affiliated light and hot spots are formed by the ultrasonic cavitation. Thereupon, these two particular parameters can be used to provide a relevant explanation for the sonocatalytic decomposition of the understudy organic dyes. Meanwhile, the pyrolysis of the H$_2$O molecules under specific situation originates hydroxyl radicals. In addition to this, sonoluminescence which is known as a phenomenon assigned to the ultrasonic cavitation, causes the creation of the light with a wide wavelength extent. Meeting the relevant wavelength of the emerged light with the Cr-MIL-101 and CoFe$_2$O$_4$ makes them exited and also causes the sonogenerated electrons and the excited holes to be appeared. To calculate the absorption band energy (E_g) of the as-prepared catalysts according to the available literatures,[27,38] the following equation can be used (5):[50]

$$(\alpha h\nu)^2 = A(h\nu - E_g) \tag{5}$$

in the above noted equation, α, h, ν, E_g and A parameters are the optical absorption coefficient, Plank constant, light frequency, absorption band gape energy, and a constant corresponded to the as-fabricated catalysts, respectively. Based on the aforementioned equation, the energy band gap (E_g) of CoFe$_2$O$_4$ and Cr-MIL-101 were estimated to be about 1.76 and 2.06 eV, respectively. Moreover, the amounts of CB and VB of CoFe$_2$O$_4$ and Cr-MIL-101 can be calculated utilizing the atom's Mulliken electronegativity definition according to the following equations (eqn (6) and (7)):

$$E_{VB} = \chi - E^e + \frac{1}{2}E_g \tag{6}$$

$$E_{CB} = E_{VB} - E_g \tag{7}$$

here E_{VB} and E_{CB} parameters are the VB and the CB potentials respectively, E^e is the energy of free electrons on the hydrogen scale (4.5 eV) and χ parameters is the absolute electronegativity of the desired semiconductors. Based on the above mentioned equations, the E_{VB} and E_{CB} amounts of Cr-MIL-101 were estimated to be +0.49 eV and −1.57 eV (ref. 27) and in contrast, the potentials for CoFe$_2$O$_4$ were calculated to be +1.9 eV and +0.14 eV (ref. 38), respectively. It is notable that the mentioned exited electrons situated at the conductions band (CB) of Cr-MIL-101 (−1.57 eV)[27] are capable to transfer straightly to the
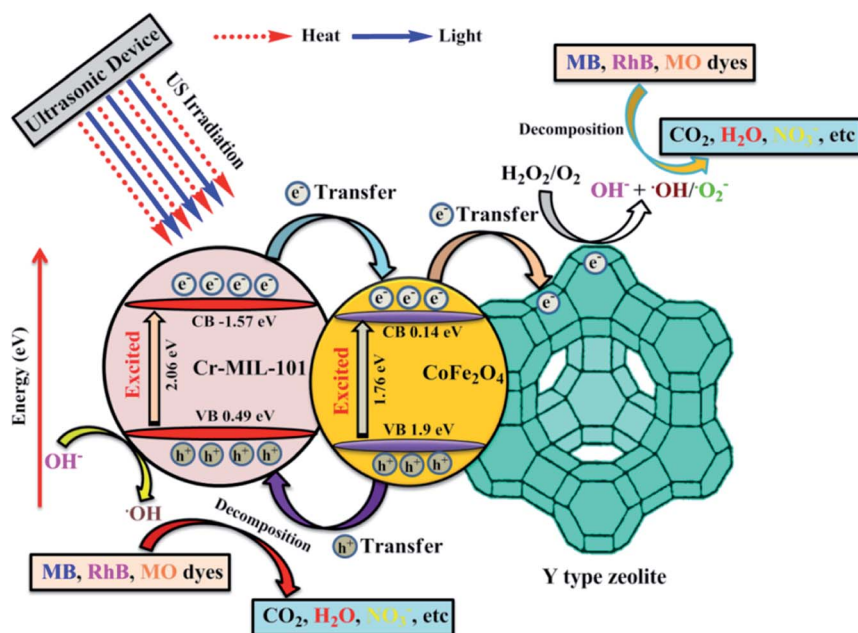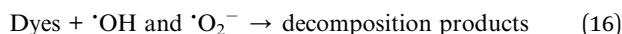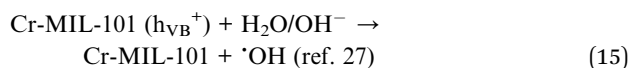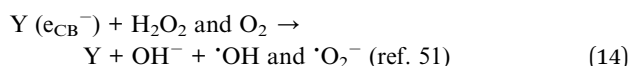

Fig. 11 A plausible mechanism for the sonodecomposition process of dye contaminants utilizing the US/H$_2$O$_2$/CoFe$_2$O$_4$@Cr-MIL-101/Y system from water solution.

CB of $CoFe_2O_4$ (+0.14 eV).[38] In contrast, the above underlined sonogenerated holes which are existent at the valence band (VB) of $CoFe_2O_4$ (+1.9 eV)[38] easily transfer to the VB of Cr-MIL-101 (+0.49 eV).[27] As a matter of fact, these perpetual migrations of the sonogenerated holes and electrons alleviate the probable aggregation and moreover enhance the charge segregation rate leading to substantially higher sonocatalytic efficiency. Besides, there is an influential phenomenon of the sonogenerated electrons migration to the surface of the $CoFe_2O_4$@Cr-MIL-101/Y zeolite nanocomposite in which the particular electron receptors are present. Considering another advantageous aspect of the synthesized catalyst nanocomposite, it is noteworthy that the zeolites[26] (in thi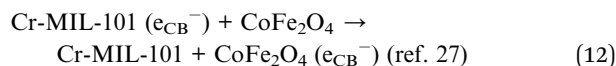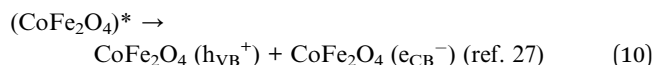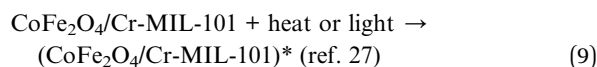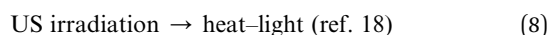s case focusing on Y type zeolite) generally are non-absorber of light in UV-Vis extent which makes them operative supports for sonocatalysis purposes. Pursuant to the above provided illustrations, the continuous motions of the sonogenerated electrons of Cr-MIL-101 and $CoFe_2O_4$ finally conduct them toward the Y type zeolite. The accommodated electrons on the surface of Y zeolite interact with H_2O_2 and O_2 from the working solution so that the resultant hydroxyl ($^{\bullet}OH$) and superoxide ($^{\bullet}O_2^-$) radicals appear, respectively. Additionally, more reactive hydroxyl radicals ($^{\bullet}OH$) are likely to be produced when H_2O_2 molecules inaugurate scavenging the specified holes (H_2O/OH^-). In consequence, the originated oxidizers respond to the involved organic dye molecules over the $CoFe_2O_4$@Cr-MIL-101/Y. This phenomenon which is attributed to the electrostatic forces triggers the creation of H_2O, CO_2 and extra salts namely NO_3^-, SO_4^{2-}, etc. as the non-toxic products of sonodecomposition reactions (eqn (8)–(16)).[15,18,27,51,52] A comprehensive plausible schematic mechanism of the entire above demonstrated process has been briefly depicted in Fig. 11.

$$US\ irradiation \rightarrow heat–light\ (ref.\ 18) \quad (8)$$

$$CoFe_2O_4/Cr\text{-}MIL\text{-}101 + heat\ or\ light \rightarrow$$
$$(CoFe_2O_4/Cr\text{-}MIL\text{-}101)^*\ (ref.\ 27) \quad (9)$$

$$(CoFe_2O_4)^* \rightarrow$$
$$CoFe_2O_4\ (h_{VB}^+) + CoFe_2O_4\ (e_{CB}^-)\ (ref.\ 27) \quad (10)$$

$$(Cr\text{-}MIL\text{-}101)^* \rightarrow$$
$$Cr\text{-}MIL\text{-}101\ (h_{VB}^+) + Cr\text{-}MIL\text{-}101\ (e_{CB}^-)\ (ref.\ 27) \quad (11)$$

$$Cr\text{-}MIL\text{-}101\ (e_{CB}^-) + CoFe_2O_4 \rightarrow$$
$$Cr\text{-}MIL\text{-}101 + CoFe_2O_4\ (e_{CB}^-)\ (ref.\ 27) \quad (12)$$

$$CoFe_2O_4\ (e_{CB}^-) + Y \rightarrow CoFe_2O_4 + Y\ (e_{CB}^-)\ (ref.\ 51) \quad (13)$$

$$Y\ (e_{CB}^-) + H_2O_2\ and\ O_2 \rightarrow$$
$$Y + OH^- + {}^{\bullet}OH\ and\ {}^{\bullet}O_2^-\ (ref.\ 51) \quad (14)$$

$$Cr\text{-}MIL\text{-}101\ (h_{VB}^+) + H_2O/OH^- \rightarrow$$
$$Cr\text{-}MIL\text{-}101 + {}^{\bullet}OH\ (ref.\ 27) \quad (15)$$

$$Dyes + {}^{\bullet}OH\ and\ {}^{\bullet}O_2^- \rightarrow decomposition\ products \quad (16)$$

4. Conclusion

For the very first time, we report a simple hydrothermal route to prepare the $CoFe_2O_4$@Cr-MIL-101/Y zeolite as a new magnetic catalyst nanocomposite. The morphological, structural and magnetic properties of the as-fabricated catalyst was characterized by several different techniques including FTIR, XRD, FESEM, EDS, EDS dot-mapping, TEM, AFM, VSM, and BET. The sonocatalytic decomposition experiments of cationic and anionic organic dyes contaminants from water solution over the $CoFe_2O_4$@Cr-MIL-101/Y were accomplished in the presence of H_2O_2 as the hydroxyl radial ($^{\bullet}OH$) origin. The influence of various parameters like irradiation time, initial dye concentration, catalyst dosage, H_2O_2 concentration, scavenger type, process type, and catalyst regeneration over the decomposition of MB, RhB and MO were evaluated. The experiments data from UV-Vis analysis showed the maximum sonodecomposition efficiency of 98.9%, 94.6% and 82% for MB, RhB and MO in the presence of $US/H_2O_2/CoFe_2O_4$@Cr-MIL-101/Y system, respectively. Besides, the reaction kinetics study of MB was fulfilled based on the first order model. The values of rate constant (k) and half-life ($t_{1/2}$) were determined as 0.0675 min^{-1} and 10.2666 min, respectively. In consequence, it is deduced that the $CoFe_2O_4$@Cr-MIL-101/Y exhibits particular and superior functionality to decompose the organic dyes compared to other catalysts such as Cr-MIL-101/Y, Y zeolite, Cr-MIL-101 and $CoFe_2O_4$.

Conflicts of interest

There are no conflicts to declare.

Acknowledgements

References

1 X. Liu, Y. Guan, Z. Ma and H. Zhou, *Langmuir*, 2004, **20**, 10278–10282.

2 V. K. Gupta and Suhas, *J. Environ. Manage.*, 2009, **90**, 2313–2342.

3 H. S. Rai, M. S. Bhattacharyya, J. Singh, T. K. Bansal, P. Vats and U. C. Banerjee, *Crit. Rev. Environ. Sci. Technol.*, 2005, **35**, 219–238.

4 S. Sadettin and G. Dönmez, *Process Biochem.*, 2006, **41**, 836–841.

5 B. J. Brüschweiler and C. Merlot, *Regul. Toxicol. Pharmacol.*, 2017, **88**, 214–226.

6 R. O. Alves de Lima, A. P. Bazoa, D. M. Fávero Salvadori, C. M. Rechb, D. de Palma Oliveira and G. de Aragão Umbuzeiro, *Mutat. Res.*, 2007, **626**, 53–60.

7 D. P. Oliveira, P. A. Carneiro, M. K. Sakagami, M. V. B. Zanoni and G. A. Umbuzeiro, *Mutat. Res.*, 2007, **626**, 135–142.

8 M. A. Behnajady, N. Modirshahla, S. Bavili Tabrizi and S. Molanee, *J. Hazard. Mater.*, 2008, **152**, 381–386.

9 Y. Zhang, L. Liang, Y. Chen, X. Chena and Y. Liu, *Soft Matter*, 2019, **15**, 73–77.

10 Y. Qin, M. Long, B. Tan and B. Zhou, *Nano-Micro Lett.*, 2014, **6**, 125–135.

11 M. Sboui, M. F. Nsib, A. Rayes, M. Swaminathan and A. Houas, *J. Environ. Sci.*, 2017, **60**, 3–13.

12 H. Eslami, S. S. Khavidak, F. Salehi, R. Khosravi, R. A. Fallahzadeh, R. Peirovi and S. Sadeghi, *J. Adv. Environ. Health Res.*, 2017, **5**, 10–15.

13 M. A. El Hajj Hassan and M. M. El Jamal, *Port. Electrochim. Acta*, 2012, **30**, 351–359.

14 H. Ghodbane and O. Hamdaoui, *Ultrason. Sonochem.*, 2009, **16**, 593–598.

15 L. Nirumand, S. Farhadi, A. Zabardastia and A. Khataee, *J. Taiwan Inst. Chem. Eng.*, 2018, **93**, 674–685.

16 A. Khataee, M. Sheydaei, A. Hassani, M. Taseidifar and S. Karaca, *Ultrason. Sonochem.*, 2015, **22**, 404–411.

17 S. Li, C. Wei, J. Wang, L. Zhang, Y. Li, Y. Li and B. Wang, *Mater. Sci. Semicond. Process.*, 2014, **26**, 438–447.

18 S. Farhadi, F. Siadatnasab and A. Khataee, *Ultrason. Sonochem.*, 2017, **37**, 298–309.

19 G. Wang, Y. Huang, G. Li, H. Zhang, Y. Wang, B. Li, J. Wang and Y. Song, *Ultrason. Sonochem.*, 2017, **38**, 335–346.

20 S. Farhadi and F. Siadatnasab, *Chin. J. Catal.*, 2016, **37**, 1487–1495.

21 Y. Min, K. Zhang, Y. Chen and Y. Zhang, *Ultrason. Sonochem.*, 2012, **19**, 883–889.

22 J. Wang, Y. H. Lv, L. Q. Zhang, B. Liu, R. Z. Jiang, G. X. Han, R. Xu and X. D. Zhang, *Ultrason. Sonochem.*, 2010, **17**, 642–648.

23 R. Darvishi, C. Soltani, M. Safari and M. Mashayekhi, *Ultrason. Sonochem.*, 2016, **30**, 123–131.

24 T. Li, L. Song and S. Zhang, *Environ. Sci. Pollut. Res.*, 2018, **25**, 7937–7945.

25 Y. Wu, L. Song, S. Zhang, X. Wu, S. Zhang, H. Tian and J. Ye, *Catal. Commun.*, 2013, **37**, 14–18.

26 M. Sadeghi, A. Zabardasti, S. Farhadi, S. Yekta and D. Mirzaei, *J. Water Process Eng.*, 2019, **32**, 100946.

27 H. T. M. Thanh, N. T. T. Tu, N. P. Hung, T. N. Tuyen, T. X. Mau and D. Q. Khieu, *J. Porous Mater.*, 2019, **26**, 1699–1712.

28 M. L. Díaz-Ramírez, E. Sánchez-González, J. R. Álvarez, G. A. González-Martínez, S. Horike, K. Kadota, K. Sumida, E. González-Zamora, M. Springuel-Huet, A. Gutiérrez-Alejandre, V. Jancik, S. Furukawa, S. Kitagawa, I. A. Ibarra and E. Lima, *J. Mater. Chem. A*, 2019, **7**, 15101–15112.

29 X.-L. Liu, R. Wang, M.-Y. Zhang, Y.-P. Yuan and C. Xue, *APL Mater.*, 2015, **3**, 104403–104407.

30 H. B. Tanh Jeazet, T. Koschine, C. Staudt, K. Raetzke and C. Janiak, *Membranes*, 2013, **3**, 331–353.

31 H. Belarbi, L. Boudjema, C. Shepherd, N. Ramsahye, G. Toquerd, J. Chang and P. Trens, *Colloids Surf., A*, 2017, **520**, 46–52.

32 E. Niknam, F. Panahi, F. Daneshgar, F. Bahrami and A. Khalafi-Nezhad, *ACS Omega*, 2018, **3**, 17135–17144.

33 M. Sadeghi, S. Yekta, H. Ghaedi and E. Babanezhad, *Mater. Chem. Phys.*, 2017, **197**, 113–122.

34 M. Dehghani, A. Tadjarodi and S. Chamani, *ACS Omega*, 2019, **4**, 10640–10648.

35 M. Sadeghi, S. Yekta, D. Mirzaei, A. Zabardasti and S. Farhadi, *J. Inclusion Phenom. Macrocyclic Chem.*, 2019, **93**, 215–227.

36 H. Ramezani, S. N. Azizi and S. R. Hosseini, *Sens. Actuators, B*, 2017, **248**, 571–579.

37 S. M. Moosavi, P. Molla-Abbasi and Z. Haji-Aghajani, *J. Mater. Sci.: Mater. Electron.*, 2016, **5**, 27–32.

38 P. Sonu, V. Dutta, S. Sharma, P. Raizada, A. Hosseini-Bandegharaei, V. K. Gupta and P. Singh, *J. Saudi Chem. Soc.*, 2019, **23**, 1119–1136.

39 M. Amiri, A. Akbari, M. Ahmadi, A. Pardakhti and M. Salavati-Niasari, *J. Mol. Liq.*, 2018, **249**, 1151–1160.

40 A. Skumiel, *J. Magn. Magn. Mater.*, 2006, **307**, 85–90.

41 A. Hannour, D. Vincent, F. Kahlouche, A. Tchangoulian, S. Neveu and V. Dupuis, *J. Magn. Magn. Mater.*, 2014, **353**, 29–33.

42 B. Abraime, A. Mahmoud, F. Boschini, M. Ait Tamerd, A. Benyoussef, M. Hamedoun, Y. Xiao, A. El Kenz and O. Mounkachi, *J. Magn. Magn. Mater.*, 2018, **467**, 129–134.

43 F. Sadri, A. Ramazani, A. Massoudi, M. Khoobi, V. Azizkhani, R. Tarasi, L. Dolatyari and B.-K. Min, *Bull. Korean Chem. Soc.*, 2014, **35**, 2029–2032.

44 R. Tabit, O. Amadine, Y. Essamlali, K. Dânoun, A. Rhihila and M. Zahouily, *RSC Adv.*, 2018, **8**, 1351–1360.

45 M. Rasouli, N. Yaghobi, S. Chitsazan and M. H. Sayyar, *Chem. Eng. Res. Des.*, 2012, **90**, 1407–1415.

46 E. M. S. Azzam, N. A. Fathy, S. M. El-Khouly and R. M. Sami, *J. Water Process Eng.*, 2019, **28**, 311–321.

47 N. Wang, L. Zhu, M. Wang, D. Wang and H. Tang, *Ultrason. Sonochem.*, 2010, **17**, 78–83.

48 W. Li, D. Wan, G. Wang, L. Lu and X. Wei, *Water Sci. Technol.*, 2016, **73**, 2345–2352.

49 S. Kamal, G.-T. Pan, S. Chong and T. C.-K. Yang, *Processes*, 2020, **8**, 104.

50 S. Singh and N. Khare, *RSC Adv.*, 2015, **5**, 96562–96572.

51 A. A. Hoseini, S. Farhadi, A. Zabardastiand and F. Siadatnasab, *RSC Adv.*, 2019, **9**, 24489–24504.

52 M. Zendehdel, Z. Kalateh and Z. Mortezaii, *J. Nov. Appl. Sci.*, 2014, **3**, 135–141.